Journal of Physics: Conference Series **2647** (2024) 082013 doi:10.1088/1742-6596/2647/8/082013

Improved double-point material point method for dynamic geotechnical problems

A Chmelnizkij

Institute of Geotechnical Engineering and Construction Management, Hamburg University of Technology, Harburger Schloßstraße 20, 21079 Hamburg

E-mail: alexander.chmelnizkij@tuhh.de

Abstract. The Material Point method is a suitable numerical method to simulate large deformations often occurring in geotechnical engineering. The Double-Point MPM (2P-MPM) extends the simulations for water-saturated materials. In the present work, a coupled dynamic formulation is used to account for coupled wave propagation in porous media in addition to large deformations. The computational cost of 2P-MPM is expensive because information between material points and grid nodes must be approximated at each time step. In conventional 2P-MPM formulations, linear shape functions are used for this approximation, leading to well-known grid crossing and loss of contact problems. We use the moving least square approximation for the 2P-MPM to handle these problems better. In addition, a parallelization approach is shown to improve the computation time, especially for large boundary value problems. The developed methods can be combined with non-saturated materials, such as fluids and dry soil, to simulate complex geotechnical issues. The performed computations of wave propagation and large deformations using the proposed methods show improved convergence behavior and increased efficiency.

1. Introduction

The 2P-MPM was proposed by [20] to simulate water-saturated porous materials. Therefore, the Standard MPM [18] was extended for two phases by introducing two sets of material points representing the solid and liquid phases. The coupling of both phases was modeled by a drag force, which serves as a momentum exchange term in the corresponding formulation. In contrast to the Single-Point MPM (1P-MPM) for saturated materials presented by [1], where a single set of material points represents the solid and liquid phases, the number of material points increases in the 2P-MPM leading to higher computational costs. This disadvantage is accepted to simulate both phases better in their individual movements. In addition, the increased computational time can be reduced by using parallelization techniques like vectorization of the data and efficient neighbor searching on regular grids. One of MPM's most significant sources of inaccuracy is the permanent transfer mapping of information between material points and nodes. The Moving Least Square Method (MLS) gave the possibility to mitigate the numerical error of the mapping and became a common approach for meshfree methods [5]. The MLS has also been successfully applied to 1P-MPM [19]. Following the same ideas, we use the MLS to 2P-MPM, where we have two instead of one set of material points [9]. Combined with different weighting functions, the accuracy of the proposed method is evaluated for a coupled wave propagation benchmark [9] using a random distribution of material points.

2. Coupled dynamic formulation

Strong Form The coupled formulation is based on the mass and linear momentum conservation of the liquid and solid phases. The resulting equations are closely related to Biot's Poroelasticity [6, 7] and the formulation presented in [12]. These formulations' detailed derivation and comparison can be found in [9]. The governing equations for the velocity fields of both phases can be written as,

$$n_s \rho_s \frac{\mathrm{D}^s \mathbf{v}_s}{\mathrm{D}t} = \mathbf{div}\left(\boldsymbol{\sigma}'\right) - n_s \mathbf{grad}\left(p_f\right) + n_s \rho_s \mathbf{b} - \overline{\mathbf{f}}_d \tag{1a}$$

$$n_f \rho_f \frac{\mathrm{D}^f \mathbf{v}_f}{\mathrm{D}t} = -n_f \mathbf{grad}\left(p_f\right) + n_f \rho_f \mathbf{b} + \overline{\mathbf{f}}_d \,. \tag{1b}$$

with

$$\mathbf{f}_d = \overline{\mathbf{f}}_d + p_f \, \mathbf{grad}(n_f) \tag{2}$$

and

$$\overline{\mathbf{f}}_d = -n_f^2 \frac{\mu}{\kappa} \left(\mathbf{v}_f - \mathbf{v}_s\right) \,. \tag{3}$$

An overview of the used variables, parameters, and constants is given in the following table.

Table 1. Parameters, constants and variables for the coupled formulation

Variables and Parameters	Description
n_s	volume fraction (soil)
n_f	volume fraction (fluid)
ρ_s	grain density
ρ_f	fluid density
$\boldsymbol{\sigma'}$	effective stress tensor
P_f	pore fluid pressure
$\mathbf{b}$	body force
$\mathbf{f_d}$	drag force
μ	dynamic viscosity
κ	intrisic premeability
C_f	compressibility (fluid)

In addition, an expression for the pore fluid pressure is obtained from the mass conservation and a linear compressibility assumption for the pore fluid.

$$\frac{\partial p_f}{\partial t} = -\frac{1}{n_f C_f}\left(\mathbf{grad}\left(n_f\right) \cdot \left(\mathbf{v}_f - \mathbf{v}_s\right) + \left(1 - n_f\right) \mathbf{div}\left(\mathbf{v}_s\right) + n_f \mathbf{div}\left(\mathbf{v}_f\right)\right) \tag{4}$$

Weak Form To obtain the weak form of equation 1a and 1b we multiply both equations by the vector-valued test function $\delta \boldsymbol{u}$ and integrate over Ω^s and Ω^f with $\Omega = \Omega^s \cup \Omega^f$. The domains

Ω^s and Ω^f are occupied by soil and the pore fluid, respectively. Under the assumption of a negligible spatial variation of the porosities n_s and n_f, we obtain [9],

$$\int_{\Omega^s}\left[n_s\rho_s\frac{\mathrm{D}^s\mathbf{v}_s}{\mathrm{D}t}\cdot\delta\boldsymbol{u}\right]\mathrm{d}\Omega=\int_{\Omega^s}\left[\left(-\boldsymbol{\sigma}'+n_sp_f\mathbf{I}\right):\nabla\delta\boldsymbol{u}\right]\mathrm{d}\Omega \tag{5a}$$
$$+\int_{\Omega^s}\left[n_s\rho_s\mathbf{b}\cdot\delta\boldsymbol{u}\right]\mathrm{d}\Omega-\int_{\Omega^s\cap\Omega^f}\left[\overline{\mathbf{f}}_d\cdot\delta\boldsymbol{u}\right]\mathrm{d}\Omega$$
$$+\int_{\partial\Omega^s}\left[\left(\boldsymbol{\sigma}'-n_sp_f\mathbf{I}\right)\mathbf{n}\cdot\delta\boldsymbol{u}\right]\mathrm{d}S\,,$$

$$\int_{\Omega^f}\left[n_f\rho_f\frac{\mathrm{D}^f\mathbf{v}_f}{\mathrm{D}t}\cdot\delta\boldsymbol{u}\right]\mathrm{d}\Omega=\int_{\Omega^f}\left[n_fp_f\mathbf{I}:\nabla\delta\boldsymbol{u}\right]\mathrm{d}\Omega \tag{5b}$$
$$+\int_{\Omega^f}\left[n_f\rho_f\mathbf{b}\cdot\delta\boldsymbol{u}\right]\mathrm{d}\Omega+\int_{\Omega^s\cap\Omega^f}\left[\overline{\mathbf{f}}_d\cdot\delta\boldsymbol{u}\right]\mathrm{d}\Omega$$
$$+\int_{\partial\Omega^f}\left[\left(-n_fp_f\mathbf{I}\right)\mathbf{n}\cdot\delta\boldsymbol{u}\right]\mathrm{d}S\,.$$

Discrete Form Using the MPM discretization [18] we obtain a system of equations, which can be written in matrix form as in [2, 20]. The nodal accelerations $(\hat{\mathbf{a}}_s)_i^t$ and $(\hat{\mathbf{a}}_f)_i^t$ at time t and node i are used here as the unknowns,

$$\left(\mathbf{M}_s^{lump}\right)_i^t\,(\hat{\mathbf{a}}_s)_i^t=\left(\mathbf{f}_s^{ext}\right)_i^t-\left(\mathbf{f}_s^{int}\right)_i^t-(\mathbf{F}_d)_i^t=(\mathbf{f}_s)_i^t\,, \tag{6a}$$

$$\left(\mathbf{M}_f^{lump}\right)_i^t\,(\hat{\mathbf{a}}_f)_i^t=\left(\mathbf{f}_f^{ext}\right)_i^t-\left(\mathbf{f}_f^{int}\right)_i^t+(\mathbf{F}_d)_i^t=(\mathbf{f}_f)_i^t\,, \tag{6b}$$

with the nodal masses and forces

$$(\mathbf{M}_s^{lump})_i=\sum_{sp=1}^{N_{sp}}m_{sp}N_i(\mathbf{x}_{sp})\;\;,\;\;(\mathbf{M}_f^{lump})_i=\sum_{fp=1}^{N_{fp}}m_{fp}N_i(\mathbf{x}_{fp})\,,$$

$$(\mathbf{f}_s^{ext})_i=\sum_{sp=1}^{N_{sp}}m_{sp}N_i(\mathbf{x}_{sp})\mathbf{b}(\mathbf{x}_{sp})+\int_{\partial\Omega_s}N_i(\mathbf{x})\left(\boldsymbol{\sigma}'-n_sp_f\mathbf{I}\right)\mathbf{n}\,\mathrm{d}S\,,$$

$$(\mathbf{f}_f^{ext})_i=\sum_{fp=1}^{N_{fp}}m_{fp}N_i(\mathbf{x}_{fp})\mathbf{b}(\mathbf{x}_{fp})+\int_{\partial\Omega_f}N_i(\mathbf{x})(-n_fp_f\mathbf{I})\mathbf{n}\,\mathrm{d}S\,,$$

$$(\mathbf{f}_s^{int})_i=\sum_{sp=1}^{N_{sp}}V_{sp}\boldsymbol{\sigma}'_{sp}\;\mathbf{grad}(N_i)(\mathbf{x}_{sp})-\sum_{fp=1}^{N_{fp}}(1-n_{fp})p_{fp}V_{fp}\,\mathbf{grad}(N_i)(\mathbf{x}_{fp})\,,$$

$$(\mathbf{f}_f^{int})_i = -\sum_{fp=1}^{N_{fp}} n_{fp} V_{fp} p_f \mathbf{I}\, \mathbf{grad}(N_i)(\mathbf{x}_{fp})\,,$$

$$(\mathbf{F}_d)_i = -\sum_{j=1}^{N_n}\sum_{fp=1}^{N_{fp}} \frac{m_{fp} n_{fp} g}{\kappa_{fp}} N_i(\mathbf{x}_{fp}) N_j(\mathbf{x}_{fp})(\mathbf{v}_{fj} - \mathbf{v}_{sj})\,.$$

In the discretization of equation 6a and 6b, we used the nodal shape functions N_i, which in the Standard MPM are chosen as triangular hat functions. Later we will replace these with MLS shape functions to increase the method's accuracy.

Time Integration To integrate equation 6a and 6b in time, the explicit forward Euler scheme is used for the nodal momentum vectors $(\hat{\mathbf{mv}})_s$ for the solid and $(\hat{\mathbf{mv}})_f$ for the liquid phase.

$$(\hat{\mathbf{mv}})_s^{t+\Delta t} = (\hat{\mathbf{mv}})_s^t + \Delta t \mathbf{f}_s^t \tag{9a}$$

$$(\hat{\mathbf{mv}})_f^{t+\Delta t} = (\hat{\mathbf{mv}})_f^t + \Delta t \mathbf{f}_f^t \tag{9b}$$

The pore pressures at the material points according to equation 4 are also obtained by finite differences discretization. While a forward difference discretizes the time derivative of the pore pressure, the velocity fields on the right-hand side can be evaluated either at time t or $t + \Delta t$, which can be obtained from equation 9a through division by the nodal masses. Here we use the velocity fields at time $t + \Delta t$, corresponding to the semi-implicit Euler method.

$$\begin{aligned} p_f^{t+\Delta t} &= p_f^t \\ &- \frac{\Delta t}{n_f C_f}\big(\mathbf{grad}\,(n_{fp}) \cdot (\mathbf{v}_f - \mathbf{v}_s) + (1 - n_f)\,\mathbf{div}\,(\mathbf{v}_s) + n_f \mathbf{div}\,(\mathbf{v}_f)\big) \end{aligned} \tag{10}$$

As the quanteties in equation 10 are evaluated at material points and the velocity fields in equation 6a and 6b are nodal values, an approximation of the divergence is needed. This is achieved by utilizing the nodal shape functions.

$$\mathbf{div}(\mathbf{v}_p) \approx \sum_{i=1}^{N_n} \mathbf{grad}(N_i)(\mathbf{x}_p) \cdot \mathbf{v}_i \tag{11}$$

Again, the spatial variation of the porosities is considered to be negligible, and therefore, $\mathbf{grad}\,(n_{fp}) \approx 0$ in equation 10 is assumed.

3. Parallelization

A parallelization concept is briefly presented here to improve the computational efficiency of the method introduced in the previous section. For more details, the reader is referred to [9].

Neighbor searching Similar to meshfree methods [5] searching algorithm is needed in MPM to identify the domain of influence of each material point. While in many meshfree methods, this domain is related to the compact support of the kernel functions, in MPM it is linked to the element size and the compact support of the nodal and material point shape functions. Therefore we need to know in which element the material points are located in each time step. We consider a regular rectangular mesh in the following.

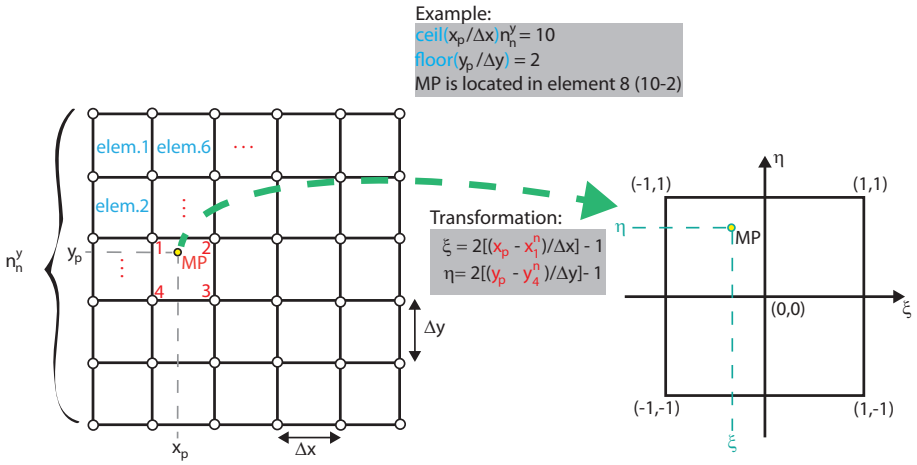

Figure 1. An example to determine the location of the material point MP and its local coordinates taken from [9]. In the case of Standard MPM, the information of the material point MP is mapped to the four nodes of the element where MP is located.

In figure 1 an example is shown to determine the location of a material point in a rectangular mesh using the ceiling and floor functions. As the compact support of the nodal shape function in the Standard MPM is equal to the neighboring elements of the considered node, only four nodes are influenced by the shown material point. Vice versa, the information of a node will be mapped to all material points located in its adjacent elements. Replacing the linear shape function with a quadratic B-Spline, which will later be used in the MLS, will increase the region of influence, as shown in figure 2.
Keeping data like the coordinates of each material point in array form allows performing the ceiling and floor commands in parallel and obtaining a multi-dimensional array including all relevant nodes. The presented searching algorithm, in combination with a vectorized implementation in MATLAB, can be found in [9]. Compared to a sequential implementation, a speedup of more than 25x was obtained for the investigated benchmarks in [9].

4. Moving Least Squares

Using linear shape functions in the Standard MPM leads to some numerical issues that will be addressed here. The linear hat function implies a C^0- inter-element continuity. Therefore differential quantities like stress or pore pressure are discontinuous at the element interfaces. This leads to an unphysical jump when a material point moves from one element to another. This well-known issue is called grid crossing and can be mitigated by the introduction of smoother shape functions. Therefore [4] proposed to smooth the shape functions using the convolution of rectangular and linear shape functions, which led to a new quadratic B-Spline type of shape

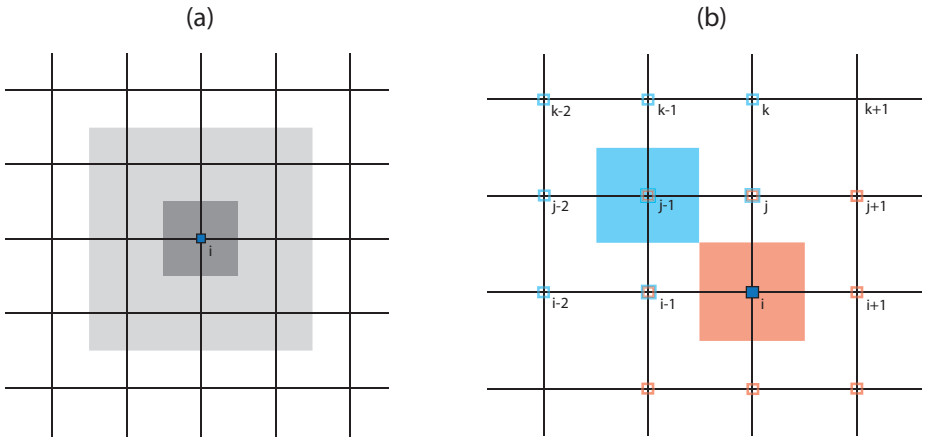

Figure 2. The region of influence of node i for a quadratic B-Spline is shown in (a). If a material point is located inside the dark or light gray area, non-zero values will be mapped from node i to it. In (b) the opposite mapping is considered. If a material point is located in the red area, its information will be mapped to the nine red-marked nodes. The same holds for the blue area.

function. In [17] the linear shape functions were replaced by higher-order B-Splines to overcome the girdcrossing problem. In the present work, we will use the MLS shape functions first introduced for MPM in [19]. The MLS [15] can approximate an arbitrary function u given by a set of n values $\mathbf{u} = (u_1\ u_2 \dots u_n)^T$ at $\mathbf{x}$ by

$$\mathbf{\Phi}^{\mathbf{MLS}}(\mathbf{x})\mathbf{u} = \sum_{i=1}^{n} \Phi_i^{\mathbf{MLS}}(\mathbf{x}) u_i \quad \text{with} \quad \Phi_i^{\mathbf{MLS}}(\mathbf{x}) = w(\mathbf{x}-\tilde{\mathbf{x}}_i)\, \underbrace{\mathbf{p}^t(\mathbf{x})\mathbf{M}^{-1}(\mathbf{x})}_{:=\mathbf{c}(\mathbf{x})^t}\, \mathbf{p}(\tilde{\mathbf{x}}_i)\,, \tag{12}$$

where $p(x) = (1\ x\ y \dots xyz \dots)^T$is a vector representing a polynomial basis of chosen order and $w(\mathbf{x}-\tilde{\mathbf{x}}_i)$ is the weighting function centred at $\tilde{\mathbf{x}}_i$. The matrix $\mathbf{M}(\mathbf{x})$is formed by the weighting functions and the polynomial bases evaluated at the given values [5]. The derivatives of the shape functions $\Phi_i^{\mathbf{MLS}}(\mathbf{x})$ can be found according to [11, 16].
To show the increased accuracy of MLS, we follow an example from [9] and reconstruct the MATLAB function *peaks*

$$z(x,y) = 3\,\mathrm{e}^{-(y+1)^2-x^2}\,(x-1)^2 - \frac{\mathrm{e}^{-(x+1)^2-y^2}}{3} + \mathrm{e}^{-x^2-y^2}\left(10\,x^3 - 2\,x + 10\,y^5\right), \tag{13}$$

from a scattered set of material points on a regular grid. We apply different weighting functions and the constant polynomial basis $p(x) = (1)$. Therefore the case of linear B-Splines corresponds to the Standard MPM. The relative L_2-error is evaluated to compare the results.

The improved approximation accuracy of MLS with smoother weighting functions is shown in figure 3. In addition to B-Splines of different order, the Wendland function according to [15] was applied.
Different choices of weighting functions allow us to change the continuity and compact support of $\Phi_i^{\mathbf{MLS}}(\mathbf{x})$, which helps to mitigate the gird crossing noise as well as a different issue often

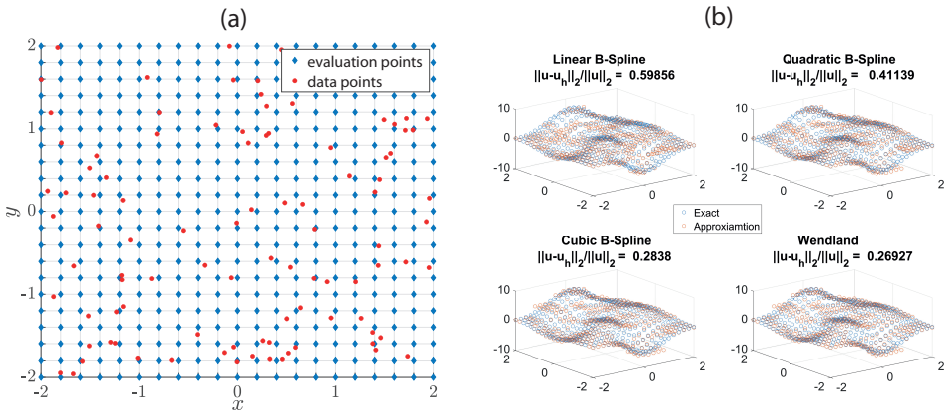

Figure 3. (a) The scattered data set(red) and the nodes(blue), where the approximation is evaluated as shown. (b) The relative L_2-error between the approximation $\mathbf{u_h}$ and the exact function given by equation 13 is compared for different weighting functions.

referred to as numerical fracture or loss of contact. As mentioned in the previous section, the region of influence is determined by the compact support of the shape functions. Once two material points move away from each other, further than this region, no interaction between them is left. This means that mesh size and the choice of weighting functions determine the fracture behavior of the material and not some constitutive model. To enlighten this issue, we use the Method of Manufactured Solutions(MMS) [13]. In particular, the example given in [19]. Therefore a solution for the displacement field of the form

$$\mathbf{u}(X,Y,t) = \begin{pmatrix} u_1 \\ u_2 \end{pmatrix} = \begin{pmatrix} B\sin(\pi X)\sin(c\pi t) \\ B\sin(\pi Y)\sin(c\pi t) \end{pmatrix} \tag{14}$$

with homogeneous boundary conditions is assumed. The necessary body forces are calculated and applied from these assumptions in calculating the numerical solution. The amplitude B can be chosen differently to mimic small and large deformations. For the case $B = 0.05$ and an element size of $h = 0.125$ as shown in [9], the Standard MPM develops a vertical and horizontal crack, as shown in the following figure.
In figure 4, the formation of a numerical crack in the Standard MPM is shown. The material along this crack loses the self-contact and behaves like a torn cloth. A convergence analysis for different weighting functions and polynomial bases is carried out in the following. The error is a time-averaged discrete L_2 error, where T_N is the number of time steps and n_p is the number of material points.

$$error = \frac{1}{T_N}\sum_{n=1}^{T_N}\left(\frac{1}{n_p}\sum_{p=1}^{n_p}\|\mathbf{v}_p^n - \mathbf{v}_{p,MMS}^n\|_2\right). \tag{15}$$

The reader is referred to [9] for material parameters and further details of the convergence analysis.

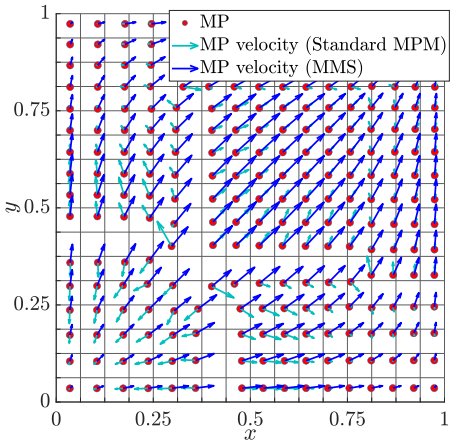

Figure 4. Numerical fracture in the Standard MPM solution for an amplitude of $B = 0.05$ and an element size of $h = 0.125$.

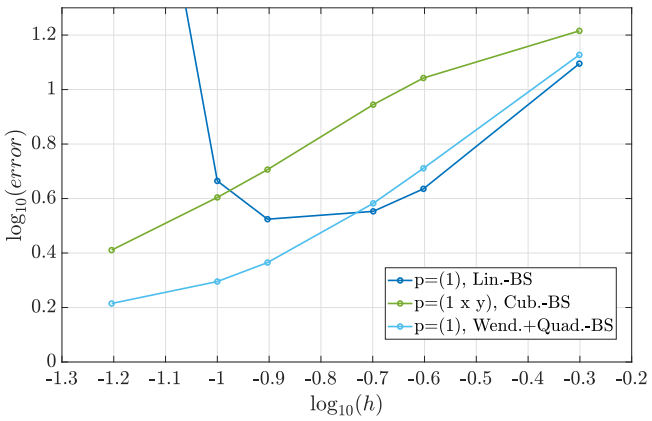

Figure 5. Comparison of MMS and numerical solutions for the case $B = 0.05$. **dark blue**: Standard MPM; **green**: Cubic B-Spline with $\mathbf{p}(\mathbf{x}) = (1\, x\, y)^t$ for nodal velocities + cubic B-Spline with $\mathbf{p}(\mathbf{x}) = (1)$; **light blue**: Wendland weighting functions with $\mathbf{p}(\mathbf{x}) = (1)$ for nodal velocities + quadratic B-Spline with $\mathbf{p}(\mathbf{x}) = (1)$ for all other variable.

The results in figure 5 show the improved convergence properties of MLS shape functions. Different combinations of weighting functions for the reconstruction of different fields, e.g., velocity, mass, stress, etc., decrease the error even further.

5. MLS for 2P-MPM

In this section, we use the MLS shape functions to improve the accuracy of the 2P-MPM. The main difference between the application of MLS to 1P-MPM and 2P-MPM is that now the mapping from material points to nodes is performed on two separate scattered sets of material points. In the following, we consider the example from [9], which represents a coupled wave propagation of a shock in a saturated column on two scattered sets of material points, one for the solid and one for the liquid phase. Different weighting functions were investigated in combination with the constant polynomial basis $p(x) = (1)$. In figure 6 the results for different

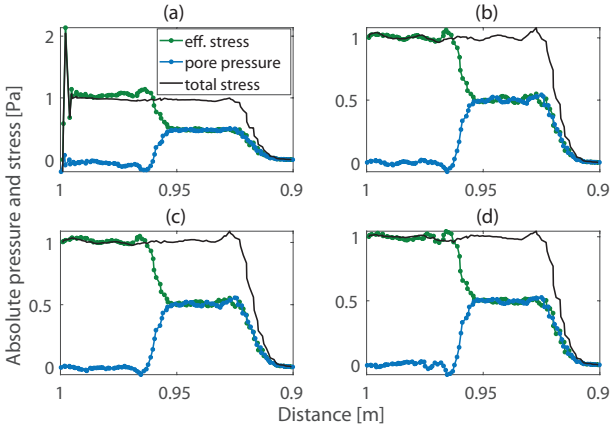

Figure 6. Comparison of different weighting functions for MLS: (a) Linear B-Spline, (b) Quadratic B-Spline, (c) Cubic B-Spline and (d) Wendland with $\mathbf{p}(\mathbf{x}) = (1)$. The discontinuity or shock propagates from left to right, increasing the stress and pressure to non-zero values. The total stress(black) is obtained as the sum of the effective stress(green) and pore pressure(blue).

MLS variations are shown. The analytical solution and detailed benchmark description can be found in [9, 10]. Again the application of MLS shape functions shows an improved convergence behavior, which is particularly clear as the total stress of the analytical solution is exactly 1 Pa behind(left) the shock. The case of linear B-Splines, corresponding to the Standard MPM, shows large oscillations in the effective stress with a maximum amplitude of over 2 Pa.
In many applications of 2P-MPM, non-vanishing gradients of porosity are considered in contrast to the shown wave propagation example. This is often used in erosion and sedimentation processes where the change of porosity serves as a transition criterion. Examples of such applications can be found in [2, 3, 8, 14, 20]. Considering a non-vanishing porosity gradient leads to additional terms in the coupled formulation, which were assumed to be negligible for the wave propagation case. The MLS could also approximate the varying scalar porosity field and its vector-valued gradient field analogous to mass and velocity, respectively. In general, the MLS replaces the linear shape functions of the standard MPM with shape functions that have a better approximation quality for scalar and vector-valued fields. From this point of view, the presented method should also work for other formulations than those presented here. This will be investigated in more detail in the future.

6. Conclusions

The presented application of MLS to MPM improved the accuracy and overcame common issues of the Standard MPM as grid crossing and numerical fracture or loss of contact. In particular, the

application to scattered sets of material points decreased the numerical error significantly. The extension to 2P-MPM showed similar behavior for shock propagation in saturated material. While different MLS approaches showed only small oscillations due to the scattered set of material points, the Standard MPM deviated strongly from the analytical solution. In addition to the accuracy analysis, a parallelization approach was suggested to improve the computational efficiency of MPM.

Acknowledgments
Funded by the Deutsche Forschungsgemeinschaft (DFG, German Research Foundation) – GR 1024/45

References

[1] Al-Kafaji I 2013 Formulation of a dynamic Material Point Method (MPM) for geomechanical problems *Fakultät für Bau- und Umweltingenieurwissenschaften der Universität Stuttgart* DOI:10.18419/opus-496
[2] Bandara S 2013 Material Point Method to simulate large deformation problems in fluid-saturated granular medium *Department of Engineering* University of Cambridge
[3] Bandara S and Soga K 2015 Coupling of soil deformation and pore fluid flow using material point method. *Computers and Geotechnics* **63** 199–214
[4] Bardenhagen S and Kober E 2004 The Generalized Interpolation Material Point Method *Computer Modeling in Engineering and Sciences* **5(6)** 477–495
[5] Belytschko, T., Krongauz, Y., Organ, D., Fleming, M., Krysl, P., 1996. Meshless methods: an overview and recent developments, Computer methods in applied mechanics and engineering 139(1-4), 3–47
[6] Biot M A 1956a Theory of propagation of elastic waves in a fluid-saturated porous solid. I. Low-frequency range *The Journal of the Acoustical Society of America* **28(2)** 168–178 DOI:10.1121/1.1908239
[7] Biot M A 1956b Theory of propagation of elastic waves in a fluid-saturated porous solid. II. Higher frequency range *The Journal of the Acoustical Society of America* **28(2)** 179–191 DOI:10.1121/1.1908241
[8] Ceccato F, Yerro A and Martinelli M 2018 Modelling soil-water interaction with the material point method. Evaluation of single-point and double-point formulations *Numerical methods in geotechnical engineering IX* CRC Press, 351–358
[9] Chmelnizkij A 2023 Regularized MPM for porous media Dissertation. *Institut für Geotechnik und Baubetrieb* Technische Universität Hamburg DOI:https://doi.org/10.15480/882.4941
[10] Chmelnizkij A, Ceccato F, Grabe J and Simonini P 2019 1D Wave propagation in saturated soils: verification of two-phase MPM *2nd International conference on the material point method for modelling soil-water-structure interaction* Cambridge UK
[11] Huerta A, Belytschko T, Fernández-Méndez S, Rabczuk T, Zhuang X and Arroyo M 2017 Meshfree Methods *Encyclopedia of Computational Mechanics Second Edition* John Wiley and Sons, Ltd DOI: https://doi.org/10.1002/9781119176817.ecm2005 1–38
[12] Jong G d J de 1956 'Wat gebeurt er in de grond tijdens het heien (Dutch)' (What happens in the soil during pile driving) *DE INGENIEUR* **25**
[13] Knupp P and Salari K 2002 Verification of Computer Codes in Computational Science and Engineering *CRC Press* DOI:10.1201/9781420035421
[14] Martinelli M and Rohe A 2015 Modelling fluidisation and sedimentation using material point method *1st Pan-American Congress on Computational Mechanics* 1–12
[15] Nealen A 2004 An as-short-as-possible introduction to the least squares, weighted least squares and moving least squares methods for scattered data approximation and interpolation. *http://www.nealen.com/projects* **130(150)** 25
[16] Nguyen V P, Rabczuk T, Borda S and Duot M 2008 Meshless methods A review and computer implementation aspects *Mathematics and computers in simulation* **79(3)** 763–813
[17] Steffen M, Wallstedt P, Guilkey J, Kirby R and Berzins M 2008 Examination and analysis of implementation choices within the material point method (MPM). *Computer Modeling in Engineering and Sciences* **31(2)** 107–127
[18] Sulsky D, Chen Z and Schreyer H L 1994 A particle method for history-dependent materials *Computer methods in applied mechanics and engineering* **118(1-2)** 179–196
[19] Sulsky D and Gong M 2016 Improving the material-point method *Innovative Numerical Approaches for Multi-Field and Multi-Scale Problems* Springer 217–240
[20] Więckowski Z 2013 Enhancement of the material point method for fluid-structure interaction and erosion. *Research project report*, Deltares.